AERODYNAMIC INTERACTION EFFECTS OF TILTROTOR EVTOL AIRCRAFT

Catharina Moreira[1] & Christian Breitsamter[2]

[1]Technical University of Munich, Chair of Aerodynamics and Fluid Mechanics
Boltzmannstr. 15, 85748, Garching bei München, Germany

Abstract

In light of recent advancements in electric aircraft systems tailored for eVTOL applications, there is a growing need for a better understanding of aerodynamic loads and their interactions for unconventional propulsion systems which must deliver both lift and thrust. Therefore, a wind tunnel model was specifically designed for investigating wing-propeller aerodynamic interactions of eVTOL aircraft, including vectored thrust mechanisms. The model encompasses capabilities for both time-averaged and time-resolved measurements of load and pressure data, and the facilities at the Technical University of Munich also enabled flow visualization with Particle Image Velocimetry (PIV). This paper offers load, pressure and flow visualization data for wing-propeller configurations, considering propeller tilt angles between 0° and 90° with 15 degree steps. It was found that Root Mean Square (RMS) values of forces measured at the propeller are lower for lower tilt angles with regard to the wing when comparing similar angles of inflow at the propeller plane. Power Spectral Densities (PSD) of total model forces show that the propeller rotation frequency and its harmonics are relevant, especially as tilt angle increased. PIV revealed significant variation in wake vortex structures depending on tilt angle.

Keywords: tiltrotor, wind tunnel, airframe-propeller interaction, propellers at incidence

1. Introduction

Innovative aircraft concepts have been proposed in the last decades in response to the escalating demand for efficient urban transportation. Urban Air Mobility (UAM) became a focal point in engineering research and has raised unique requirements for aircraft development. Electric vertical take-off and landing (eVTOL) vehicles have attracted attention in this context due to their potential to fulfill specific UAM requirements by combining the efficiency of fixed-wing aircraft with the agility of rotary-wing vehicles. Nevertheless, the entry into service of eVTOL aircraft still faces technical challenges. Several of the proposed solutions are aerodynamically complex and deviate from conventional operating conditions [1], for example with propellers operating in strongly interactional flow fields and/or under non-axial inflow, resulting from the introduction of features such as distributed propulsion and wings or propellers capable of tilting mid-flight.

Various areas of eVTOL research and development highlight interactional aerodynamics as a key factor, such as noise prediction [2], trajectory optimization [3] and aeroelastic stability [4]. The aerodynamics of interacting propellers [5, 6] and isolated propellers operating at incidence [7, 8, 9] have been studied previously. For example, [10] investigated propellers operating at incidence angles from 0 to 180 degrees, finding influences in thrust coefficient and also in-plane force coefficients resulting from the non-axial inflow. Their results point to a strong amplitude of blade passing frequency (BPF). Specifically considering wing mounted propellers operating in traditional cruise configuration, effects on the wing cause by rotating blades (asymmetrically for downgoing and upgoing blades) have been reported by [11]. These experiments had isolated propellers, multirotor configurations, or wingtip mounted propellers [12] as focal points, thus providing valuable but limited insight into interactional

aerodynamics of tilting propulsion systems, particularly when lifting surfaces such as wings are considered.

Dynamic coupling between a wing and propeller was a topic of interest already in the 1960s in connection to whirl flutter investigations [13]. The topic of whirl flutter has attracted attention also in the context of eVTOL aircraft due to its relevance in structural design and safety of tiltrotor vehicles, as highlighted by [14, 15]. An effort to numerically predict vibratory loads is described in [16], while [15] evaluated numerical sensitivities to parameters for whirl flutter prediction using experimental data.

Experimental methods remain an invaluable resource to gain understanding for complex aerodynamics and validate newly developed simulation tools. Recently, several authors have employed experimental flow visualization techniques to explore topics related to eVTOL development. PIV flow visualization was used by [17] to study ground effects of a hovering quad tiltrotor aircraft. Furthermore, In 2021 [18] investigated side by side propellers using phase-locked PIV visualization, whereas [19] conducted a study on the effects of blade-vortex interaction which included PIV techniques. Lastly, [20] investigated a full scale tiltrotor model, obtaining not only pressure data but also temperature maps to analyze local effects on the wing via infrared thermography.

With this in mind, a subscale model of a generic eVTOL aircraft was designed, including a wing, pylon and leading-edge tilting propeller. This investigation aims to contribute to the understanding of aerodynamic interactions by providing comprehensive time-resolved load and pressure experimental data, improving current understanding of eVTOL transition behavior by direct analysis while also providing extensive data to validate and expand predictive tools.

The presented work is done within the LuFoVI-2 project ETHAN (Safe and Reliable Electrical and Thermal Networks for Hybrid-Electric Propulsion Systems) funded by the German Federal Ministry of Economics and Climate Protection (Bundesministerium für Wirtschaft und Klimaschutz).

This paper is structured as follows: first, the experimental setup and testing conditions are introduced in Section 2. Then, in Section 3, pressure coefficient distributions over selected wing airfoil sections are analyzed for different model configurations, including the isolated wing, the wing with pylon support structure but no propeller and the full model assembly with propeller at various tilt angles. Next, in Section 4, a comparison of isolated and full model configurations is carried out, focusing on comparison of root mean square (RMS) values for propeller aerodynamics loads and frequency analysis of isolated and full model configurations. Finally, Section 5 presents PIV images of the flow in the wake of the model (two chord lengths behind the wing) for a direct comparison of various propeller tilt angles.

2. Experimental Setup

A modular eVTOL model was developed, built and tested at the Technical University of Munich. Detailed information about the design was given in [21], while a summary is given in the following.

The eVTOL model is a reconfigurable test bench designed to enable testing of a wide range of possible aircraft architectures including vectored propulsion concepts and lift and cruise concepts. The current setup consists of a hollow, rectangular wing and a pylon assembly, the latter of which supports the propulsion system with a five-bladed propeller and the tilting mechanism responsible for switching between different configurations in similar fashion to a tiltrotor eVTOL aircraft. The model is illustrated in Figure 1.

The half wing model is sized 1.1 m in span (peniche excluded) and features a NACA4418 airfoil with 290 mm chord length, resulting in a half wing model aspect ratio of 3.79. Beneath the wing, at the section closest to the floor, the model is isolated from incoming airflow by a 3D printed fairing (peniche) to reduce the influence of ground effects, especially the wind tunnel floor boundary layer, on the measurements. This fairing is 0.1 m tall and it is assembled mechanically detached from

measurement systems by design, to ensure that loads in this section are not recorded during testing campaigns. The model is installed on a turntable in the wind tunnel test section in such a way that the turntable surface is in contact with the peniche (indicated by floor level in Figure 1) and therefore some structural components and the underfloor load cell are located below the tunnel test section. Two adjustable angular parameters of the model are indicated in Figure 1: the propeller tilt angle (TA) with regard to the wing, adjusted by the linear actuator, and the wing angle of attack (AoA), adjusted by the turntable.

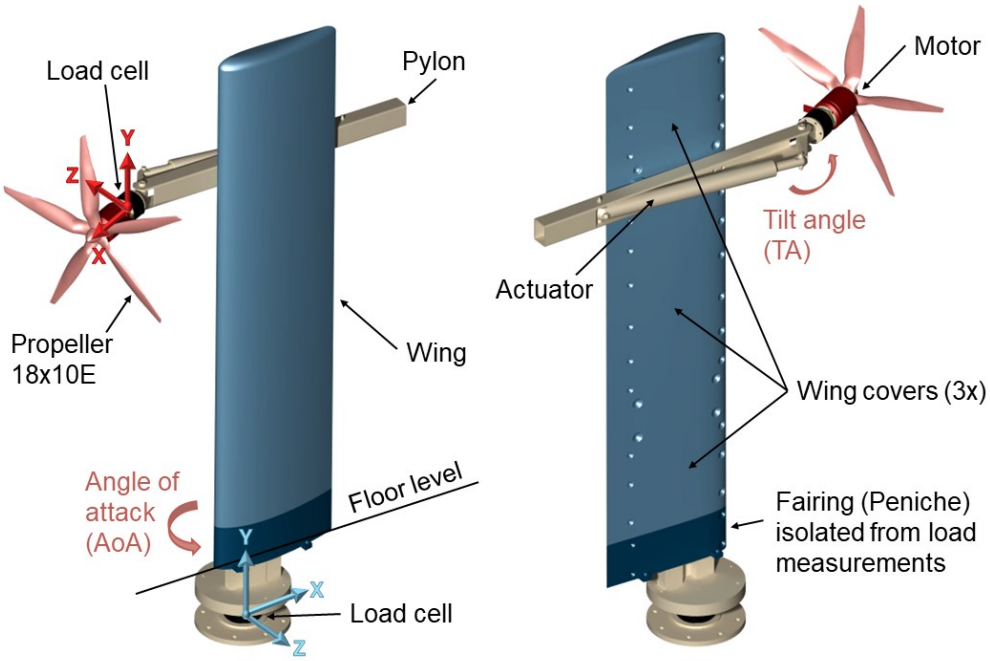

Figure 1 – Digital model of the test bench and its components, viewed from top surface (left) and bottom surface (right) of the wing.

Two load cells are available for time-resolved load measurements. Their location and reference axes are indicated in Figure 1. One load cell is located underneath the wind tunnel test section floor level and supports the entire model assembly. This cell can measure forces up to 5 kN in X and Z axes (see Figure 4) and 15 kN in Y axis, as well as moments up to 250 Nm. Its accuracy class is 0.2% relative to full scale and the X axis is oriented along the wing chord. The other load cell is located directly behind the electric motor that drives the propeller and can measure forces up to 500 N (Y and Z axes) /2000 N (X axis) and moments up to 20 Nm (Y and Z axes)/40 Nm (X axis). Its accuracy class is 0.5% relative to full scale and the X axis is oriented as the propeller rotation axis.

Additionally, the wing includes a total of 207 pressure taps, distributed over 9 airfoil sections across the span, of which 192 taps provide stationary and 20 taps transient pressure data. The 20 transient sensors were distributed in four groups of five sensors, located at the four outermost wing sections, which are closest to the wing tip. These sections are directly located in the wake of the propeller. An illustration of the distribution of stationary and transient sensors is provided in Figure 2. Sections 1-4 are sensored exactly as shown, whereas for the remaining five sections, all 23 taps on each section are stationary. The location of taps with regard to chord along the wing surface is the same for all sections. Section 5 is positioned in the middle of the wing, while sections 1-4 are located on each side of the pylon at 0.5 R and 0.78 R with regard to the propeller blades (reference diameter 18 in / 457 mm). The pressure tubes are routed through the hollow inside of the wing, along with all other cables for measurement and power systems, in order to keep the wing surface undisturbed. The inside of the wing is accessible by detaching three covers located on the bottom surface.

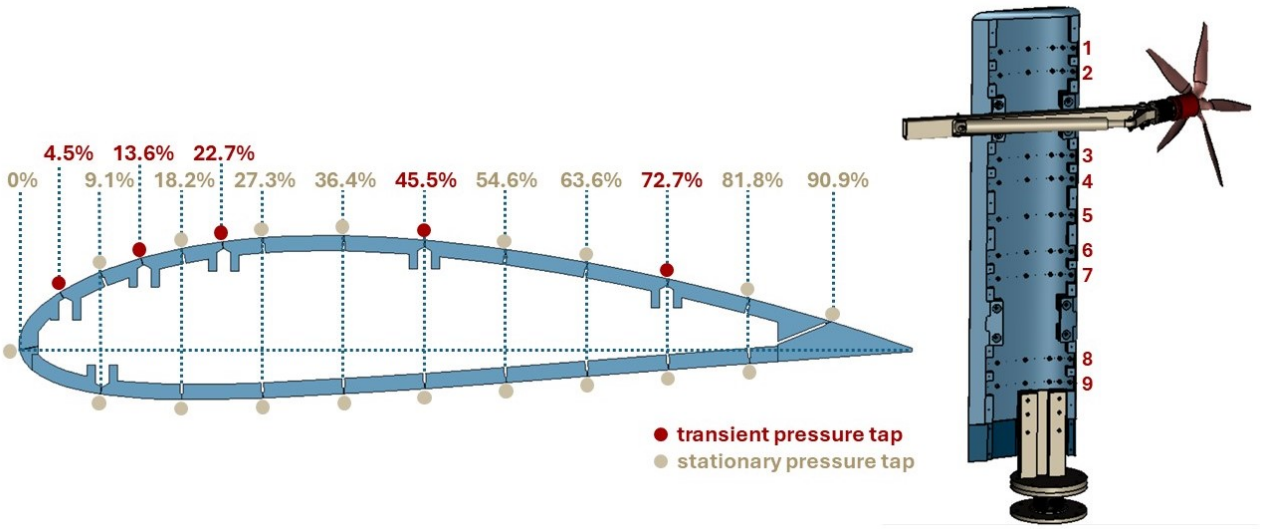

Figure 2 – Representative wing section with location of pressure taps in percentage of wing chord (left) and location of each section on the wing, shown here without bottom surface covers (right).

In order to better understand interaction effects, other configurations were tested for comparison. The full assembly of wing, pylon and propeller is named wing-propeller (WP) and is shown in Figure 3a. The wing in isolation (clean wing - CW) was also measured in the wind tunnel, as well as a wing-pylon assembly without the propeller blades (no propeller - NP). The latter is shown in Figure 3b. Furthermore, the same five-bladed propeller used for the eVTOL model was also tested in isolation in the wind tunnel (isolated propeller - IP), supported by a steel rod as shown in Figure 3c. This setup is similar to the one described in [22] with the difference that the motor was replaced in order to deliver higher power outputs necessary for the five-bladed propeller. This means that the entire assembly of propeller, motor, load cell and adapter plates is the same in both the isolated setup (IP) and in the full eVTOL (WP) model.

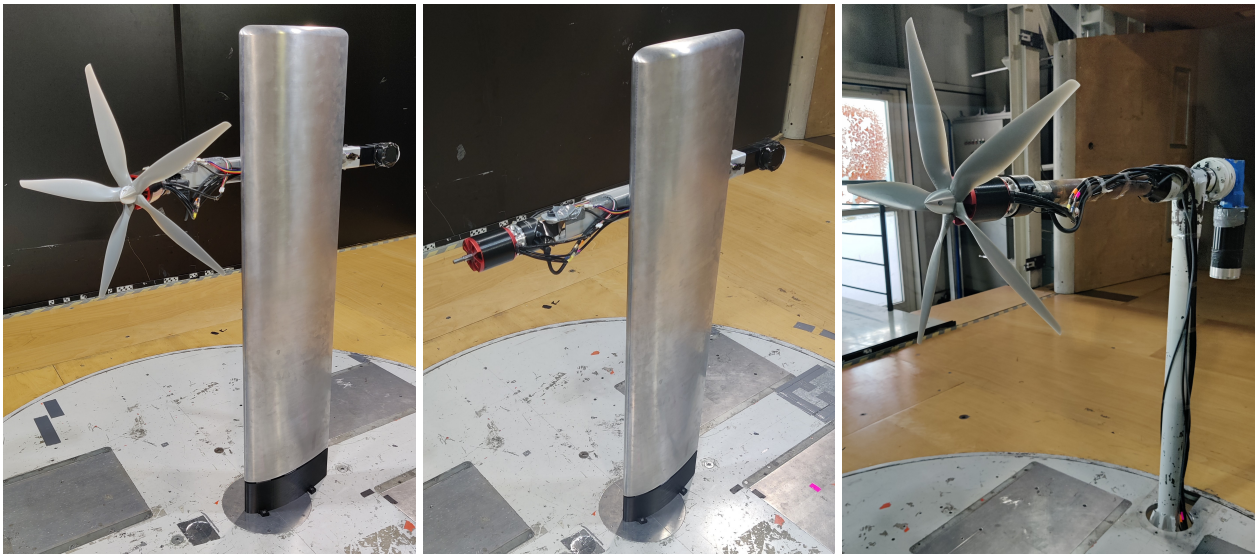

(a) Wing-propeller eVTOL model. (b) Wing-pylon (no propeller). (c) Isolated propeller test bench.

Figure 3 – Variations of the experimental setup in the wind tunnel.

All investigations in this work that include a propeller were done with the same custom five-bladed 18 in (457 mm) diameter propeller operating at nominal 4000 RPM, which corresponds to approximately 0.3 Mach at the blade tip. Its blade geometry is the same as the commercially available two-bladed

APC 18x10E propeller. Propeller rotation was inboard-up. An optical sensor placed at the motor provided 1/revolution signals, used for post processing data. The propeller is driven by a 4 kW brushless DC electric motor supplied with 48 V DC and controlled by an electronic speed controller. An overview of testing conditions is provided in Table 1. In addition, images of the model at two TA configurations are shown in Figure 4 to illustrate the differences.

Table 1 – Overview of model variations and testing conditions.

Model Type	**AoA (Wing)**	**TA (Propeller)**	**Wind Speed**
Wing-Propeller (WP)	[-5°, 0°, 5°, 10°, 13°, 15°, 18°, 20°, 23°, 25°]	0° - 90°; 15° steps	17 m/s
Clean (isolated) Wing (CW)	-10° - 25°; 2.5° steps	——	17 m/s
No Propeller (NP) Wing-Pylon	-10° to 25°; 2.5° steps	0°, 45°, 90°	17 m/s
Isolated Propeller (IP)	——	0° - 90°; 15° steps	[0, 17] m/s

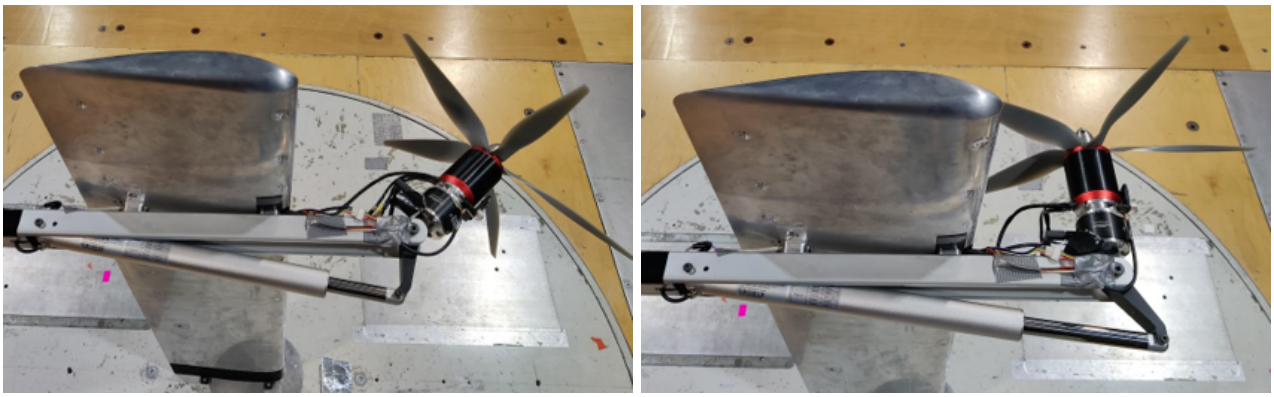

(a) WP, TA 45. (b) WP, TA 90.

Figure 4 – Model as mounted in the wind tunnel, illustrating two different TA configurations.

A small adaptation of the current setup in comparison to the description in [21] is a change to the height of the trip dots placed in proximity to the wing leading edge to induce a turbulent boundary layer on the wing model (from 400 μm zigzag tape in the reference to 290 μm trip dots in this work). Details on the change and the effect of the newly introduced trip dots are given in Section 3.

Lastly, images of the flow field in the wake of the wing-propeller eVTOL model were obtained via stereoscopic particle image velocimetry (Stereo-PIV) measurements. The measurement section was perpendicular to the wing chord and positioned two chord lengths (580 mm) behind the trailing edge. For this study, AoA was fixed at $0°$ and wind speed at 17 m/s. Eight different configurations were tested, including seven wing-propeller configurations with TA $0°$ to $90°$ (steps of $15°$) and one no propeller (NP) configuration. For each configuration, three separate Stereo-PIV measurements were performed and combined in order to expand the measured plane and enable the visualization of the entire propeller wake.

The Stereo-PIV system is located next to the wind tunnel test section and illuminates the measurement plane with a double-pulsed neodymium-doped yttrium aluminum garnet (Nd:YAG) laser, which has a maximum power of 325 mJ per pulse and a wavelength of 532 nm. Two scientific complementary metal oxide semiconductor (sCMOS) cameras with a resolution of 2560 × 2160 pixels are placed

up- and downstream of the measurement plane, which has dimensions of 0.45 m × 0.21 m. The cameras measure 400 image pairs per measured cross-flow section with 15 Hz sampling frequency. Seeding for the measurements is provided by Di-Ethyl-Hexyl-Sebacate (DEHS) with a diameter of approximately 1 μm.

All wind tunnel investigations were carried out at the TUM-AER Wind Tunnel A, which is a Göttingen type wind tunnel with test section dimensions 1.8 x 2.4 x 4.8 m (width x height x length). The tunnel can reach up to 65 m/s with an open test section and has turbulence intensities in each coordinate direction below 0.4%.

3. Pressure Analysis

Previous studies [21] with this model featured a zigzag tape placed near the leading edge in order to ensure that the boundary layer on the model is turbulent, since low Reynolds numbers at the scaled wing model could result in laminar flow conditions that are not comparable to real scale aircraft. For the current U_∞ of 17 m/s, however, the tape was thicker than required and therefore negatively impacted the pressure distribution over the airfoil section. Thus, the tape was replaced with new trip dots, which have a height of 290 μm. Figure 5 shows a comparison of pressure coefficient C_P distribution over one section of the wing, considering the previously tested methods (free transition, 150 μm trip dots and zigzag tape) and the new trip dots.

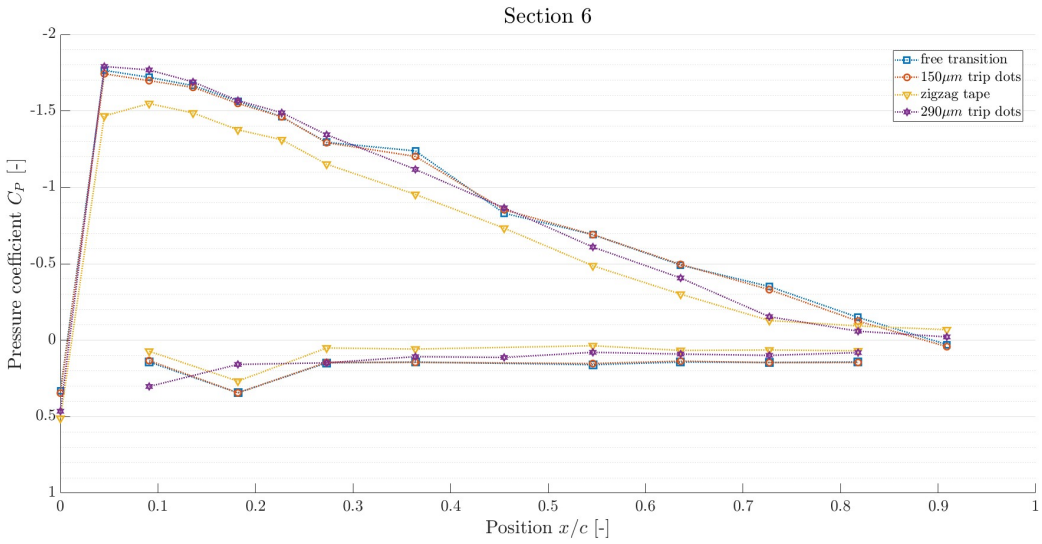

Figure 5 – C_P over an airfoil section with different boundary layer tripping strategies.

It is noticeable that both in free transition and with dots of 150 μm there is a decrease in pressure coefficient around 0.35 x/c that indicates the presence of a laminar separation bubble. The zigzag tape effectively eliminated that issue, at the cost of decreased ΔC_P over the entire section. The pressure distribution with the new dots presents no sign of laminar effects while also maintaining the desired ΔC_P.

Considering the airfoil sections illustrated in Figure 2, a WP configuration with TA 0 and the fact that the propeller rotation of the model is inboard-up, it is known that the airfoil sections 1 and 2 are located behind downward moving blades, sections 3 and 4 behind upward moving blades, and sections 5 to 9 are located in undisturbed segments of the wing (in free stream). The pressure distributions shown in Figure 6 enable a comparison between CW, NP and WP configurations. Sections 6 to 8 have been omitted because these sections showed results similar to the undisturbed section 9.

Small variations in C_P in sections 2 and 4, which are closest to the mounting position of the pylon, can be observed when comparing isolated wing CW and wing-pylon NP cases. Sections 1 and 2 are closest to the wingtip of the model and therefore affected by the downgoing propeller blades. This shifts the suction peak of the airfoil section further back towards the trailing edge, while C_P at the bottom wing surface close to the trailing edge becomes more negative.

Sections 3 and 4 are affected by the upgoing blades, deviating from baseline pressure distribution with a higher stagnation pressure coefficient at the leading edge and more negative suction peaks. This effect is more pronounced in section 3 when compared to 4. Section 5 seems to be slightly affected by the propeller, although this section is not positioned behind it, showing a slight increase in C_P at the bottom wing surface close to the leading edge. This effect is not seen anymore in sections 6 to 9, which have C_P values comparable to the baseline of CW and NP configurations. These observations are in line with literature results [11].

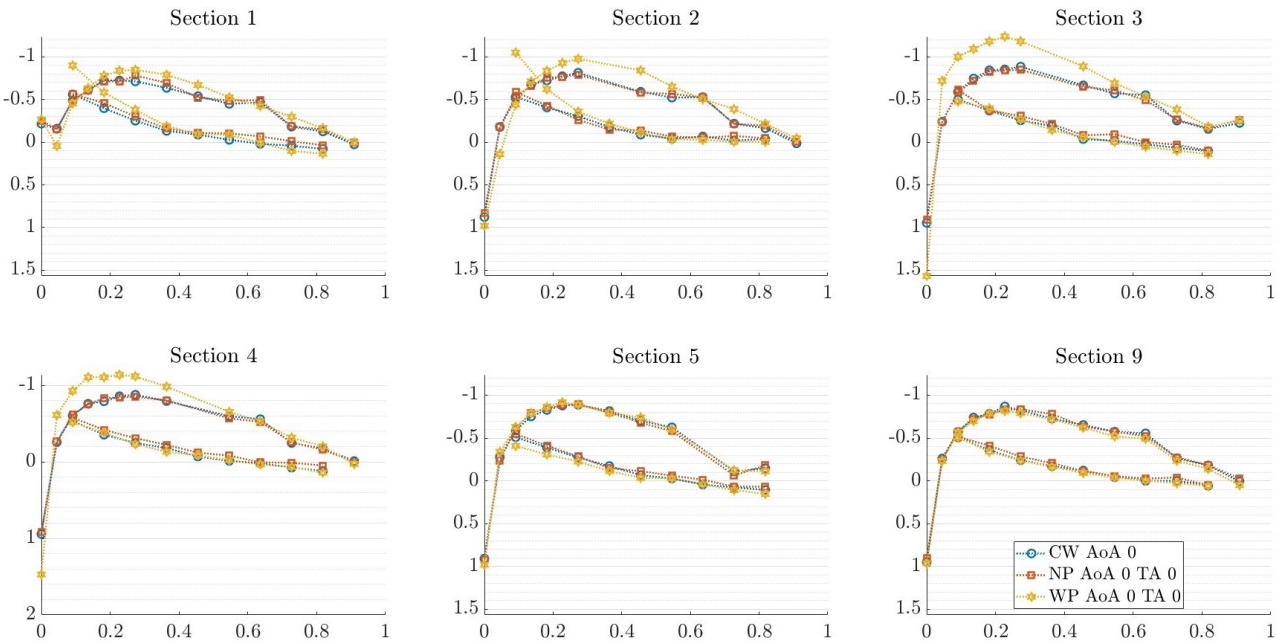

Figure 6 – Distribution of pressure coefficients along 6 airfoil sections on the wing for three different model configurations (CW, NP AoA 0 TA 0 and WP AoA 0 TA 0)

Effects of higher TA values on pressure distribution can be evaluated by analyzing Figure 7. Compared to the baseline CW, it is clear that sections 1 and 2 are affected by the forward moving blades and the propeller wake, having positive C_P values for over 20% of the section upper surface, whereas the wing bottom surface presents negative C_P. The lift generation on these sections is clearly negatively affected. The observations refer to both TA 45 and TA 90, although effects are more pronounced for TA 90, especially in section 2. Sections 3 and 4 are affected by the backward moving blades and the propeller wake, showing lower suction peaks (in absolute values), especially at section 3, and negative C_P at the bottom wing surface as well. In turn, sections 5 to 9 show pressure distributions similar to the CW and NP baselines.

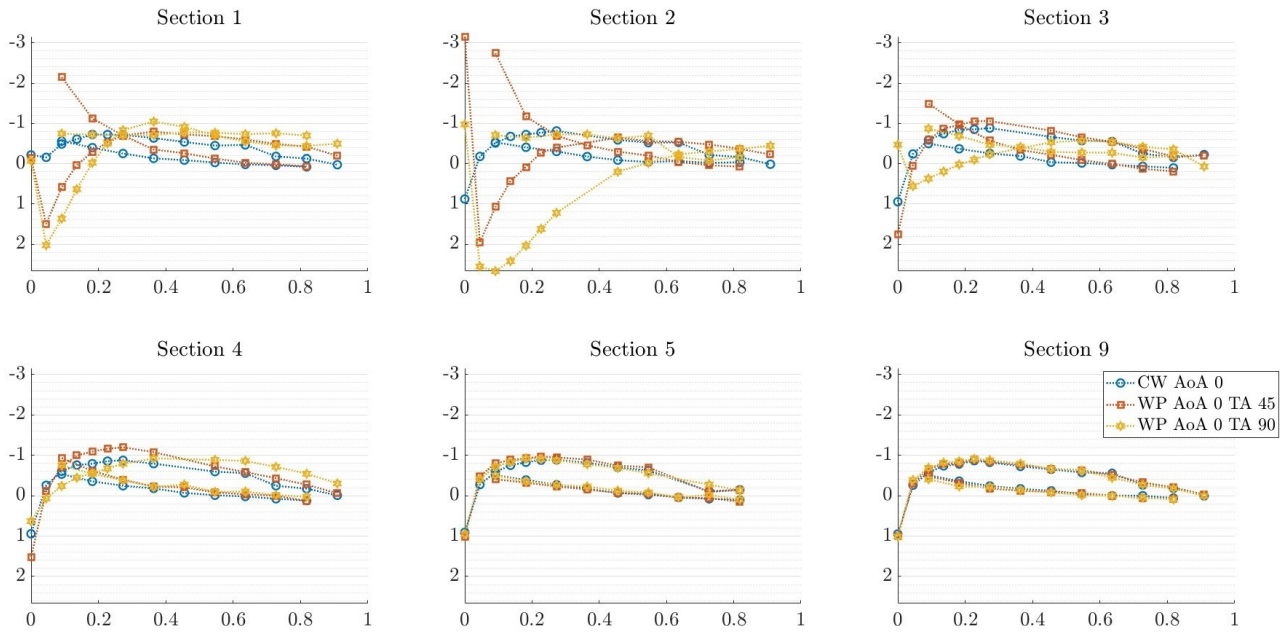

Figure 7 – Distribution of pressure coefficients along 6 airfoil sections on the wing for three different model configurations (CW, WP AoA 0 TA 45 and WP AoA 0 TA 90).

4. Load Analysis

It is particularly important to consider amplitudes and frequencies of load oscillations in the structural design of vehicles with propulsion systems that operate in non-axial inflow conditions. Transient data obtained in this study from the model load cells enable a frequency analysis by providing Power Spectral Density (PSD) distributions of measured force signals over the frequency spectrum up to approximately 4 kHz.

Average loads of the eVTOL model have been addressed in previous work. In [21], it was shown that the propeller loads in higher TA configurations lead to an increase in total model lift coefficient, as the propulsion system now contributes to system lift, and this effect is intensified as TA increases, as expected. Following the same principle, drag coefficients for the entire assembly show the influence of propeller thrust partially vectored forward, with all configurations except TA 90 showing more negative drag coefficients than the baseline CW.

Additionally, an estimation of the average forces acting solely on the wing in the WP model assembly was obtained by subtracting loads measured at the load cell location behind the propeller from total model loads obtained by the underfloor load cell, accounting for the coordinate system change between them, which is dependent on TA. Thus, a comparison of CW and calculated wing loads in WP configuration is enabled and was also reported in [21]. This comparison revealed the opposite trends as the full model for the wing operating in the interactional flow field in WP configuration, meaning that lift coefficients for the wing were lower in WP configuration than when the wing was tested in isolated (CW) configuration, with the exception of TA 0, which showed a slight increase in lift coefficient, which is in agreement with pressure distribution results. Additionally, drag coefficients of the wing, in turn, were higher in WP configuration than isolated, except for TA 90.

To analyze oscillatory behavior, load signals can be transformed into zero-mean signals and compared via Root Mean Square (RMS) values. By shifting signals to oscillate around zero instead of their original mean value a comparison of oscillatory behavior is enabled, without including variations in average magnitude of loads into the analysis. In the same manner that CW and WP are compared to gain insight into how the wing behaves in undisturbed flow versus under the influence of the propul-

sion system, the propeller operating in WP configuration can be compared with an isolated propeller setup based on the Angle of Inflow (AoI). For WP configurations, the latter represents the position of the propeller with regard to the wind and can be obtained as the sum of model AoA and propeller TA, whereas for the IP configuration the TA is also the AoI. Figure 8 shows the variation of RMS for each force measured by the load cell behind the propeller with AoI for both IP and WP configurations. RMS values are normalized by the static thrust (no wind) of the isolated propeller, $F_X = 40.4\ N$, and are therefore shown in relative values. Results are colored according to thrust coefficient C_T.

For all three axes of the propeller load cell, measured loads show a double trend in WP configurations, with higher and lower values of RMS for the same AoI, and this split is not related to C_T, since both trend lines have measurements with wide varying C_T values. All in-plane forces (F_Y and F_Z) have higher RMS values in WP configuration than isolated propeller measurements. Figure 9 shows the same RMS data, now plotted against model AoA. Although the concept of AoA does not apply to the IP experimental setup, IP results are shown at AoA 0 simply to facilitate comparison. It becomes clear that the two trend lines in AoI are two groups with regard to AoA. Model configurations with high AoA and low TA might have the same inflow angle at the propeller plane than low AoA and high TA configurations, but they present generally lower force RMS values starting at approximately AoA 13°.

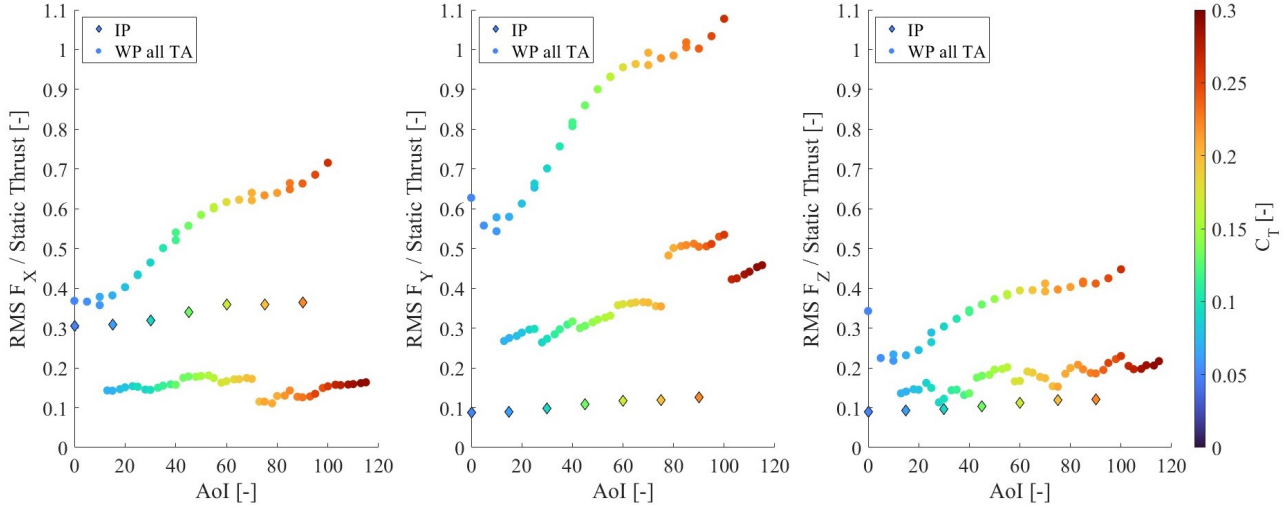

Figure 8 – Experimental RMS values relative to static thrust for propeller forces in IP and WP setups over angle of inflow, colored by mean thrust coefficient C_T.

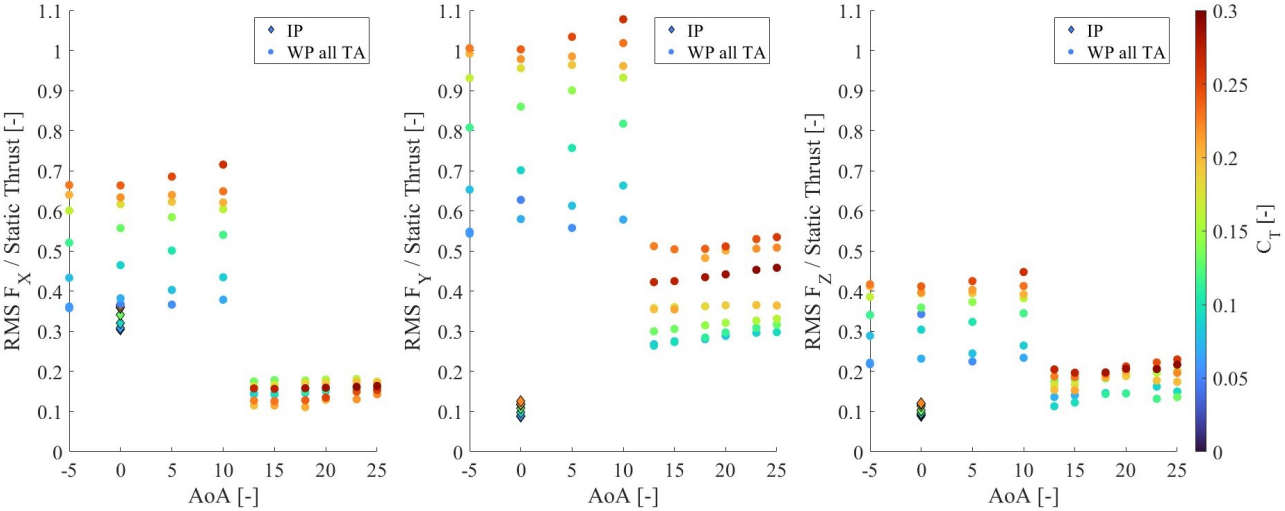

Figure 9 – Experimental RMS values relative to static thrust for propeller forces in IP and WP setups over WP model angle of attack, colored by mean thrust coefficient C_T.

Time-resolved load signals also enable a frequency analysis. In the following, PSD of force signals for different configurations are compared. Figure 10 provides the maximum spectrum available for four different configurations, namely CW, NP with tilted motor assembly at TA 90, and WP with the rotor at TA 0 and TA 90, all of them at AoA 5°. The rotational frequency of the electric motor and its harmonics are often referred to as engine orders. These are identified in the figure with dashed red lines and labels, where 1P (1 per revolution) is the first engine order, (4000 RPM or 66.67 Hz), 2P the second (133.3 Hz) and so on. The experimental setup in this work was operated with a five bladed propeller and thus has 5P, the fifth engine order, as the blade passing frequency (BPF).

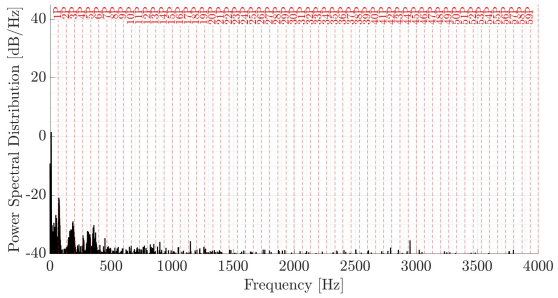

(a) CW, AoA 5.

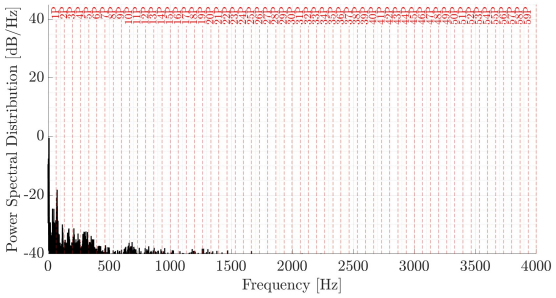

(b) NP, AoA 5, TA 90.

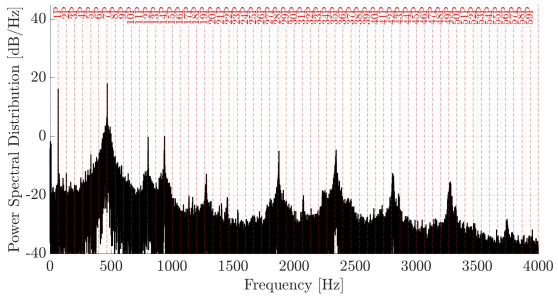

(c) WP, AoA 5, TA 0.

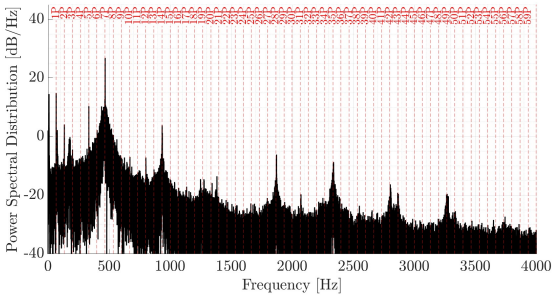

(d) WP, AoA 5, TA 90.

Figure 10 – Power Spectral Density of model force F_Z (wing axes) over frequency range up to 4 kHz for different configurations. Engine orders represented by red dashed lines. $U_\infty = 17m/s$.

It is noticeable that both configurations without a propeller in operation (CW and NP) show low levels of power for the frequencies above 500 Hz, whereas this is not the case for WP configurations, which have a higher power level across all resolved frequencies and several identifiable peaks.

Previous investigations by the authors with isolated propellers reported in [22] suggest that BPF and the motor rotational frequency (first engine order) present peaks in PSD amplitude as TA increases, also reported in the literature by [10]. Additionally, the former reference also reported peaks in harmonics of the rotational frequency, and particularly a peak at the 14th harmonic which appeared to relate to the electric motor used in the experimental setup. Considering the previous experimental setup could resolve frequencies up to 1500 Hz, it was unclear whether higher harmonics of the fourteenth engine order would be measured. Also for this reason, the sampling frequency for the current studies was increased to 8 kHz and enables therefore a higher frequency resolution.

The current wind tunnel model has a different electric motor than the setup in [22], however, with the same number of poles. It is noticeable that all engine-on configurations have amplitude peaks at the seventh engine order regardless of aerodynamic conditions. This effect is likely related to an interference, whether mechanical or electromagnetic, of the driving motor itself. Some distributions include harmonics of the seventh engine order, such as 14, 28, 35, 42 and 49, which are visible in Figure 10.

Considering the frequency range up to 350 Hz, further differences between the isolated wing and the wing-propeller model can be identified. Figure 11 provides spectral distributions for the isolated wing and two WP configurations, all at the same AoA.

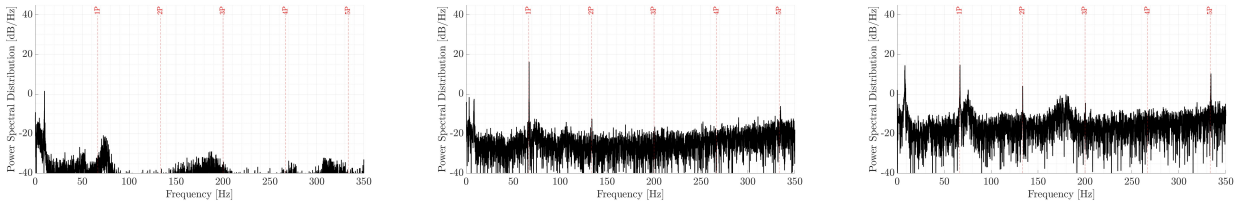

(a) CW, AoA 5. (b) WP, AoA 5, TA 0. (c) WP, AoA 5, TA 90.

Figure 11 – Detail of PSD for F_Z (wing axes) up to 350 Hz and three model configurations. Engine orders represented by red dashed lines. $U_\infty = 17m/s$.

The isolated wing shows a dominant amplitude peak around 10 Hz and further, broader increases in amplitude at approximately 75 and 180 Hz. These frequencies do not align with specific engine orders and seem to relate to the vibrational modes of the wing itself. In fact, considering a comparison of PSD over a range of AoA (see Figure 12) it seems that these frequencies are dominant for the isolated wing across the entire range of AoAs, while amplitudes increase with increasing AoA. In comparison, the two WP configurations in Figure 11 present distinct peaks at 1P, 2P and 5P and their amplitudes increase with the propeller tilting from TA 0 to TA 90.

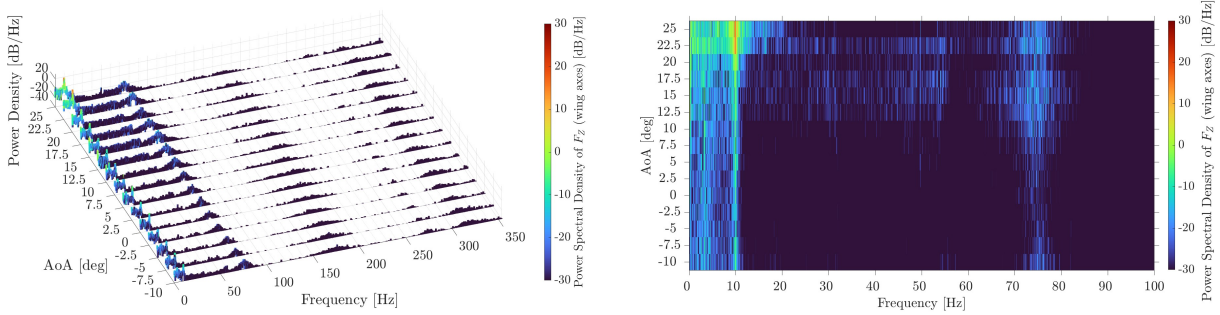

(a) Perspective view. (b) Top view.

Figure 12 – PSD of F_Z (wing axes) for the isolated wing (CW) over a range of AoA. $U_\infty = 17m/s$.

These results are in line with frequency spectra obtained for in-plane forces F_Y and F_Z (propeller axes) obtained in isolated propeller (IP) measurements. PSDs of these forces for a range of TA are shown in Figure 13. Amplitude peaks are present at all five first engine orders, with 1P as the dominant frequency for all TA and the higher order frequencies becoming more relevant as the flow deviates from the propeller rotational axis with increasing TA, with 5P featuring the second highest amplitude in this range for the TA 90 configuration. The prominence of the first engine order is likely related to an imbalance of the propeller. The narrow nature of amplitude peaks related to the propeller complicate their identification from the top view.

A comparison of WP forces F_Z and F_X (wing axes) over different TAs at AoA 0° is shown in Figure 14. The increase in power over a broad range of frequencies when compared to isolated conditions is immediately noticeable, especially in the region between 4P and 5P. Also clearly noticeable is the clear dominant 1P both on X and Z axes. Similarly to the isolated propeller cases, engine orders 2, 3, 4 and 5 show higher amplitudes as TA is increased. The peaks identified in CW configuration can also be seen in WP, especially at TA 90.

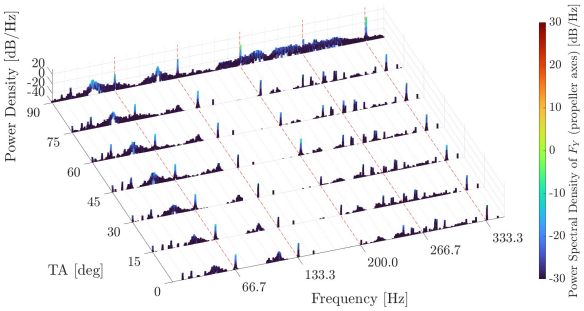

(a) F_Y propeller, perspective view.

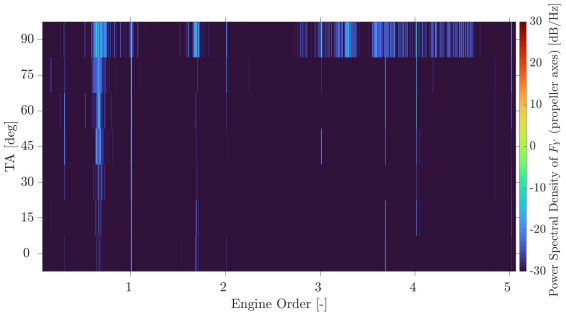

(b) F_Y propeller, top view.

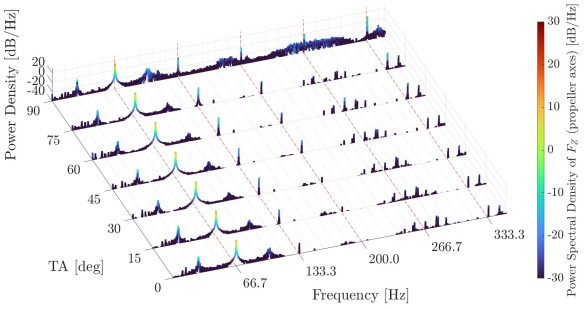

(c) F_Z propeller, perspective view.

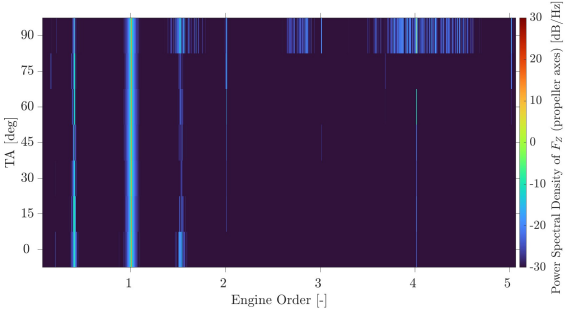

(d) F_Z propeller, top view.

Figure 13 – PSD over TA for in-plane forces in propeller axes, IP configuration. Engine orders marked in red dashed lines; order 5 is equivalent to 333.3 Hz.

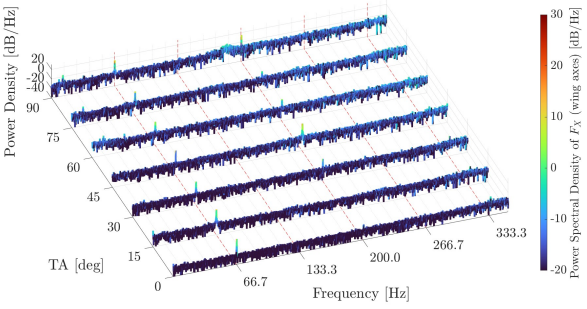

(a) F_X, wing axes. Perspective view.

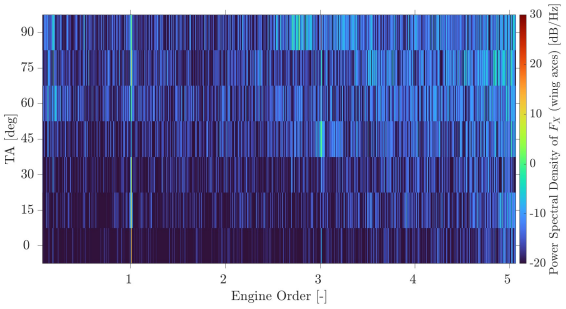

(b) F_X, wing axes. Top view.

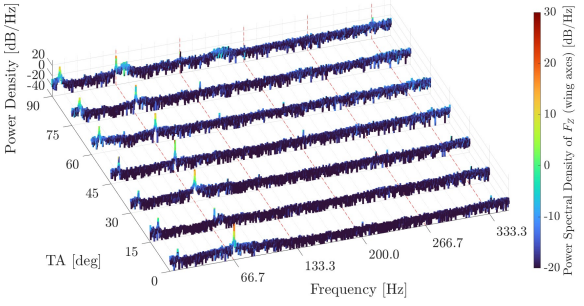

(c) F_Z, wing axes. Perspective view.

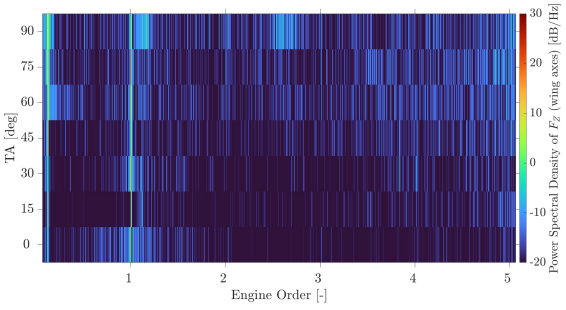

(d) F_Z, wing axes. Top view.

Figure 14 – PSD over TA for WP configuration, AoA 0.

5. Flow Visualization

Stereo-PIV measurements were carried out at a plane located two chord lengths (c) behind the trailing edge of the model wing, in order to gain insights into the effects of propeller TA on the flow. The setup is shown in Figure 15, while Figure 16 shows normalized axial velocity and Figure 17 normalized axial vorticity for all TAs considered, while AoA remained constant at 0°.

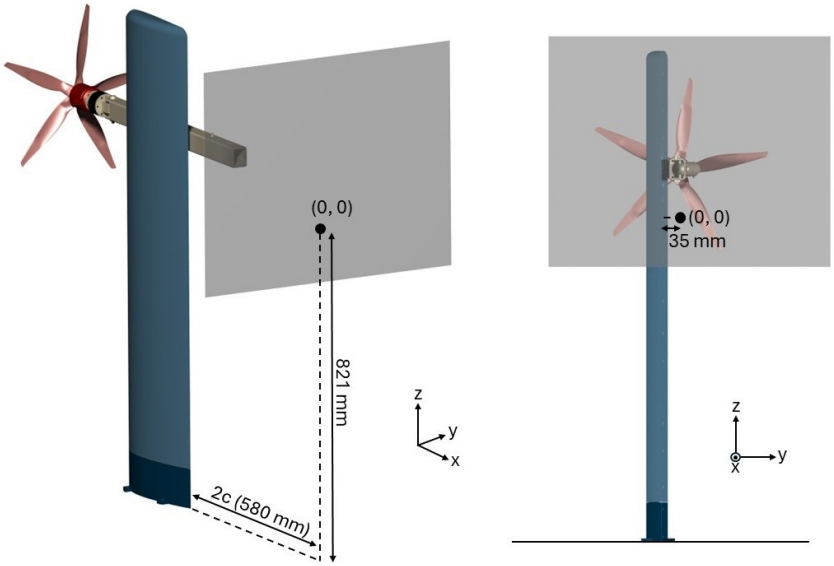

Figure 15 – Schematic representation of PIV measurement plane, represented in translucent gray color, and PIV coordinate system. Perspective view (left) and axial view from trailing edge (right).

Color levels are kept constant to facilitate interpretation of the images. Therefore certain zones with values higher or lower than the limits of the color levels appear as grayed out zones. Vorticity was normalized with propeller diameter D, which aligns with the methodology encountered in the literature [18]. The model wing profile is cambered, so this is not a zero-lift configuration. Additionally, the image triggering was not phase-locked with the propeller, meaning the results shown here are averaged over several propeller rotations.

Analyzing both normalized axial velocity and vorticity in tandem, the results show the presence of a wingtip vortex, particularly noticeable for the NP setup. Still considering NP, a region of disturbed flow likely caused by the presence of the pylon can be identified. With the propeller operating at TA 0, an increase in axial velocity in the wake of the propeller is visible, however with a smaller region of influence behind the top surface of the wing (negative y axis) as compared to the bottom surface.

As TA increases to 15 and 30 TA, the region of influence behind the top surface of the wing expands along the z axis (span-wise), whereas the increase in axial velocity in the region behind the bottom surface of the wing is intensified and reaches a maximum at TA 30. The well defined region of high values of normalized axial vorticity at TA 0, likely connected to tip vortices from the propeller blades, expands at TA 15 and TA 30. A second vortex near the wingtip seems to be present at TA 30 and then merge with the wingtip vortex starting at TA 45 and above.

For TA 45 and TA 60 it is still possible to identify zones of increased axial velocity in the propeller wake, while this effect is degenerated at TA 75 and TA 90. Specifically for TA 90, a zone of decreased axial velocity behind the wingtip, where the propeller blades are moving forward towards the leading edge, and a zone of increased velocity closer to the mid of the wing, where the propeller blades are moving backwards towards the trailing edge, can be identified. Vorticity results, in turn, suggest the formation of two counter-rotating vortex systems behind the upper surface of the wing, which are possibly formed as the propeller wake encounters the partial blockage created by the wing upper surface, as previously indicated by the positive pressure coefficients observed in Figure 7.

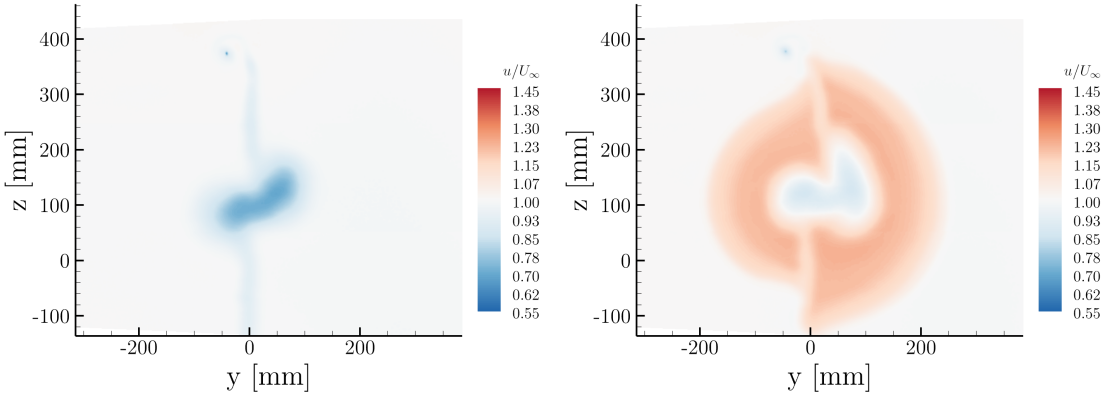

(a) NP. (b) 0 TA.

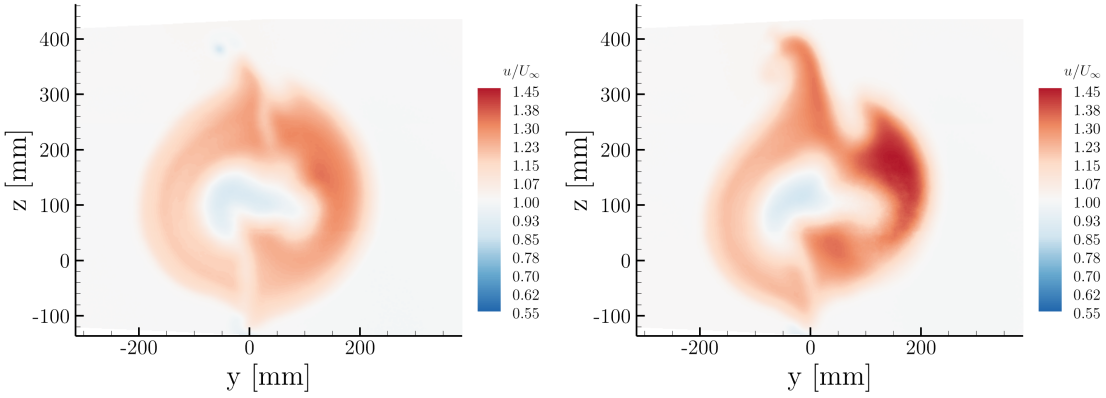

(c) 15 TA. (d) 30 TA.

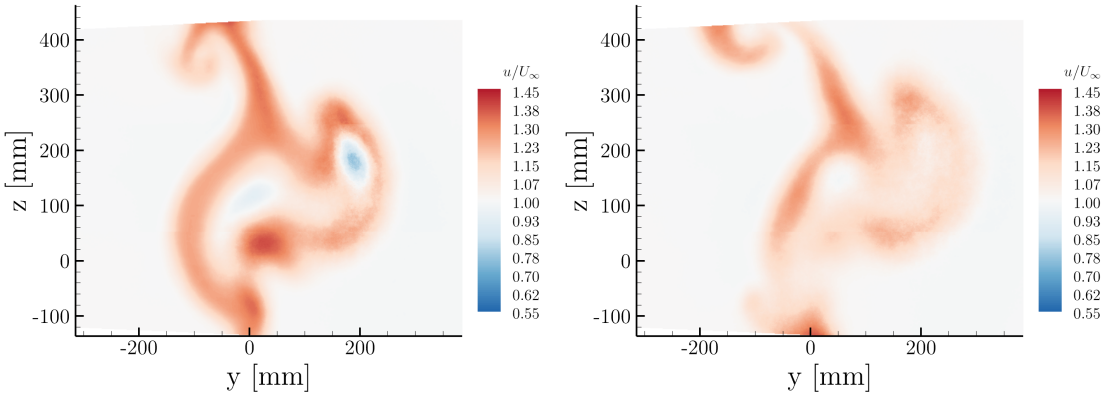

(e) 45 TA. (f) 60 TA.

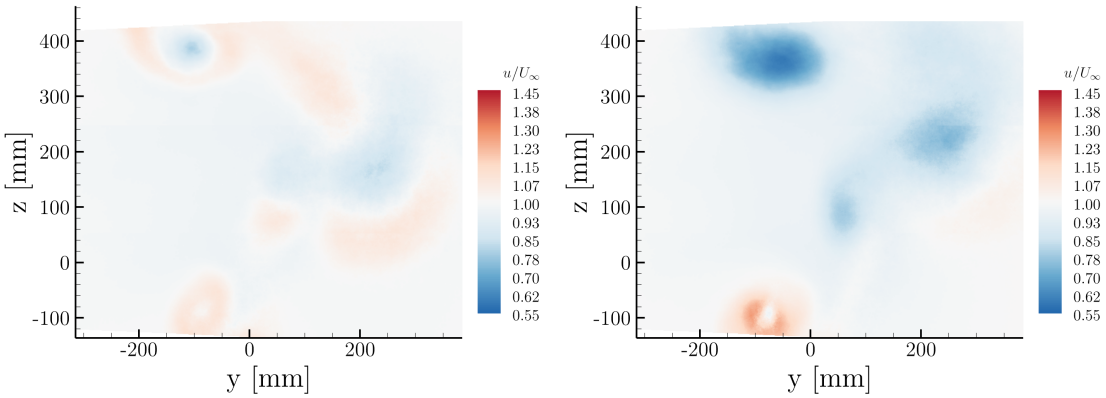

(g) 75 TA. (h) 90 TA.

Figure 16 – Normalized velocity u/U_∞ two chord lengths behind the model, PIV results.

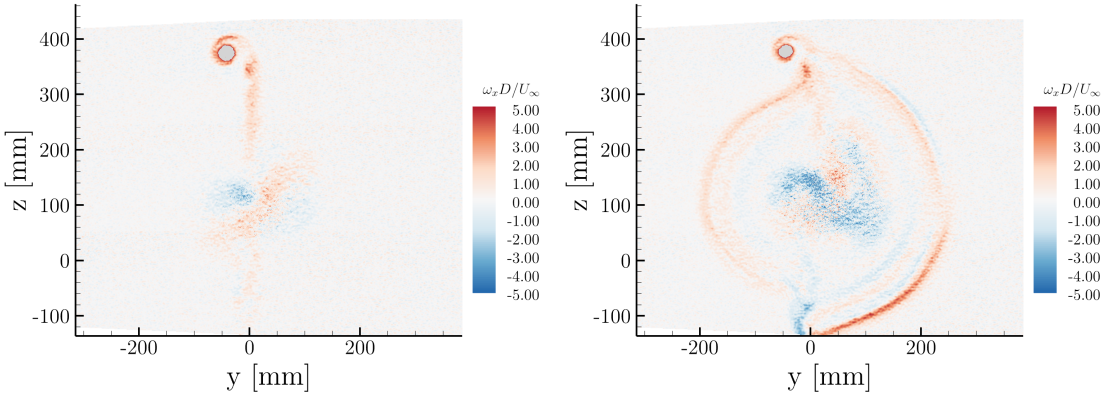

(a) NP. (b) 0 TA.

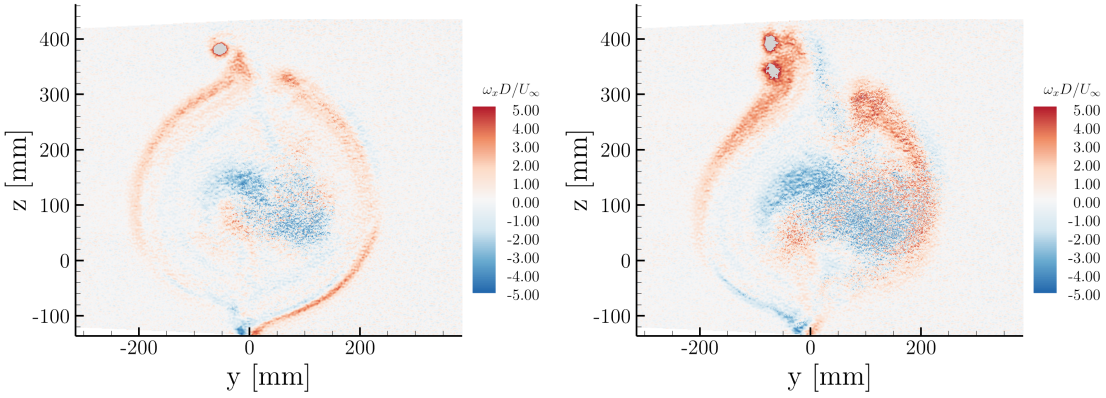

(c) 15 TA. (d) 30 TA.

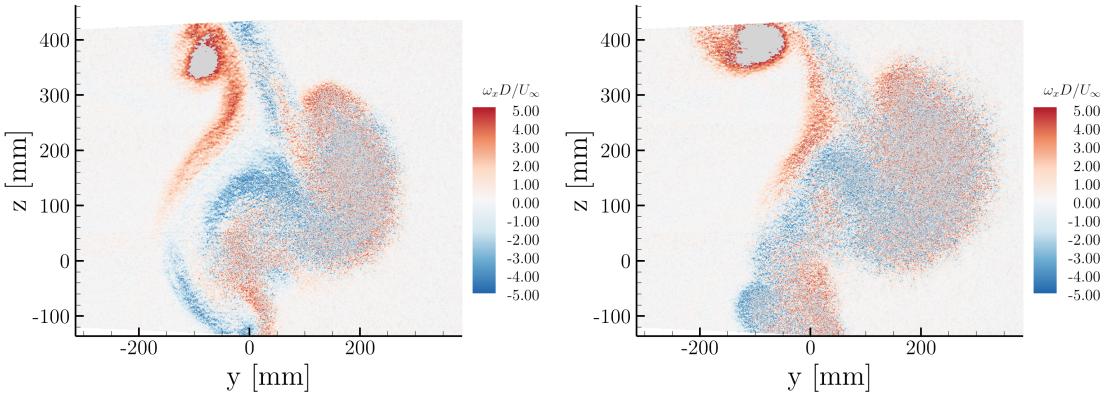

(e) 45 TA. (f) 60 TA.

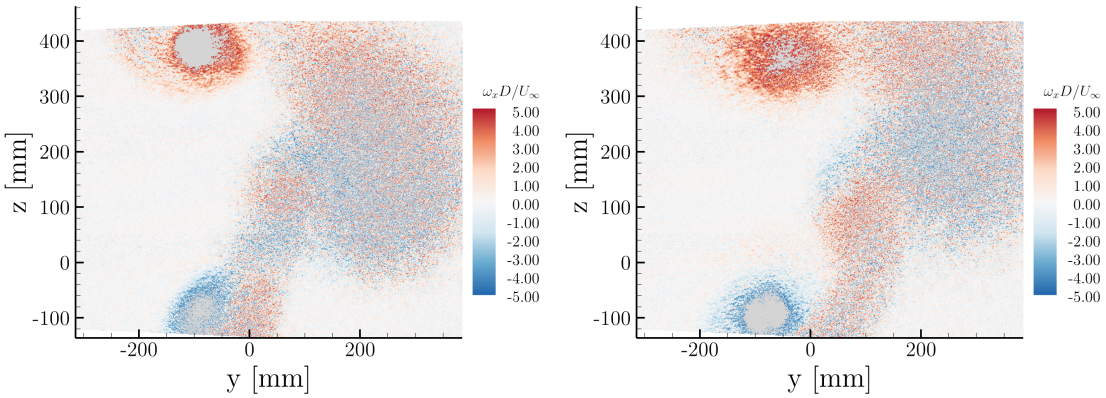

(g) 75 TA. (h) 90 TA.

Figure 17 – Non-dimensional axial vorticity $\omega_x . \frac{D}{U_\infty}$ two chord lengths behind the model, PIV results.

6. Conclusions

This work investigated the aerodynamic interactions of a tiltrotor eVTOL aircraft through wind tunnel testing of a scaled half wing model. The test setup included time-resolved load measurements, static pressure measurements and Particle Image Velocimetry (PIV). The work was focused on the effects of propeller tilt angle (TA) and wing angle of attack (AoA) on aerodynamic loads and pressure distributions, as well as wake formation.

The key findings can be summarized as follows:

1. Pressure distributions at several airfoil sections over the wing showed that, when in cruise configuration, the propeller positively influences wing sections behind upward moving blades while negatively affecting wing sections behind downward moving blades with regard to lift generation. This partially positive influence is reduced and eventually eliminated as propeller tilt angle (TA) increases to hover configuration (TA 90), with wing suction peaks on both sides of the propeller negatively affected by its wake.

2. Effects of non-axial inflow on the Root Mean Square (RMS) of forces measured behind a propeller operating in wing-propeller configuration are not only dependent on the angle of the propeller plane to the free stream incoming airflow, but also on the angle of attack (AoA) of the wing. A wing-propeller model configuration with high AoA and low propeller TA had lower propeller force RMS values in all three axes if compared to a configuration with low AoA and high TA that results in the same angle of inflow at the propeller plane.

3. Total forces on the model show increased levels of power spectral density not only at the motor rotational frequency (1P) and the Blade Passing Frequency (BPF = 5P) but also other harmonics of these frequencies, including 2P, 3P and 4P, especially at higher propeller tilt angles. Higher order frequency peaks (7P and multiples) were present in all measurements and are suspected to be caused by the electric motor.

4. Stereo-PIV measurements in the wake of the model (two chord lengths behind the wing) show the presence of a wingtip vortex and propeller wake with increased axial velocity at low tilt angles. As the TA is increased, the region of influence of the measured disturbances increased and a second vortex near the wingtip was identified at TA 30, which appears to merge with the wingtip vortex at higher tilt angles. For the hover configuration (TA 90), two vortex regions with corresponding zones of increased/decreased axial velocity can be identified, suggesting the interaction of the propeller wake with the wing surface leads to the formation of two counter-rotating vortex systems.

The experimental results reported here provide insights into aerodynamic interaction effects over different eVTOL vehicle configurations and can be used to support design efforts of eVTOL aircraft and validate numerical analysis and prediction tools, particularly to ensure safe and efficient operation during flight transition phases.

7. Contact Author Email Address

catharina.moreira@tum.de

8. Acknowledgements

This work was funded by the German Federal Ministry for Economic Affairs and Climate Action *(Bundesministerium fuer Wirtschaft und Klimaschutz)* within the LuFo VI-2 project ETHAN (Safe and Reliable Electrical and Thermal Networks for Hybrid-Electric Propulsion Systems, FKZ: 20L2103B).

9. Copyright Statement

References

[1] B. M. Simmons and P. C. Murphy. Wind tunnel-based aerodynamic model identification for a tilt-wing, distributed electric propulsion aircraft. In *AIAA Scitech 2021 Forum*, Virtual Event, 2021. American Institute of Aeronautics and Astronautics.

[2] W. Bao, W. Wang, X. Chen, H. Zhang, and Q. Zhao. Numerical analyses of aeroacoustic characteristics of tiltrotor considering the aerodynamic interaction by the fuselage in hover. *Aerospace Science and Technology*, 141:108558, 2023.

[3] S. S. Chauhan and J. R. R. A. Martins. Tilt-wing evtol takeoff trajectory optimization. *Journal of Aircraft*, 57(1):93–112, 2020.

[4] A. Cocco, S. Mazzetti, P. Masarati, S. Van't Hoff, and B. Timmerman. Numerical whirl-flutter analysis of a tiltrotor semi-span wind tunnel model. *CEAS Aeronautical Journal*, 13:923–938, 2022.

[5] C. R. Russell and S. Conley. The multirotor test bed - a new nasa test capability for advanced vtol rotorcraft configurations. 2020.

[6] T.C.A Stokkermans. *Aerodynamics of propellers in interaction dominated flowfields: An application to novel aerospace vehicles*. Ph.D. Dissertation, 2020. OCLC: 8692979511.

[7] M. Cerny and C. Breitsamter. Investigation of small-scale propellers under non-axial inflow conditions. *Aerospace Science and Technology*, 106:106048, 2020.

[8] M. Cerny, N. Herzog, J. Faust, M. Stuhlpfarrer, and C. Breitsamter. Systematic investigation of a fixed-pitch small-scale propeller under non-axial inflow conditions. Deutsche Gesellschaft für Luft- und Raumfahrt - Lilienthal-Oberth e.V., 2018.

[9] M. Stratton and D. Landman. Wind Tunnel Test and Empirical Modeling of Tilt-Rotor Performance for EVTOL Applications. In *AIAA Scitech 2021 Forum*, VIRTUAL EVENT, 2021. American Institute of Aeronautics and Astronautics.

[10] B. Theys, G. Dimitriadis, T. Andrianne, P. Hendrick, and J. De Schutter. Wind tunnel testing of a vtol mav propeller in tilted operating mode. In *2014 International Conference on Unmanned Aircraft Systems (ICUAS)*, pages 1064–1072, 2014.

[11] L.L.M. Veldhuis. Review of propeller-wing aerodynamic interference. icas 2004-6.3.1. In *24th International Congress of the Aeronautical Sciences, Yokohama, Japan*, pages –, 2004.

[12] A. Zanotti, L. Menini, A. Savino, D. Grassi, and L. Riccobene. Experimental investigation of wing-propeller aerodynamic interaction in evtol configurations. *Aerospace Science and Technology*, 152:109348, 2024.

[13] R.M. Bennet and S.R. Bland. *Experimental and analytical investigation of propeller whirl flutter of a power plant on a flexible wing*. NASA, NASA Langley Research Center, Technical Note TN-D-2399, 1964.

[14] C. Koch. Parametric whirl flutter study using different modelling approaches. *CEAS Aeronautical Journal*, 13(1):57–67, 2022.

[15] H. Kang, J. Shen, and A. R. Kreshock. Validation of comprehensive analysis for tiltrotor whirl flutter predictions. *Journal of Aircraft*, 54(4):1566–1570, 2017.

[16] M. Gennaretti, M. M. Colella, and G. Bernardini. Prediction of tiltrotor vibratory loads with inclusion of wing-proprotor aerodynamic interaction. *Journal of Aircraft*, 47(1):71–79, 2010.

[17] K. Chen, Z. Shi, S. Tong, Y. Dong, and J. Chen. Aerodynamic interference test of quad tilt rotor aircraft in wind tunnel. *Proceedings of the Institution of Mechanical Engineers, Part G: Journal of Aerospace Engineering*, 233(15):5553–5566, 2019.

[18] A. Zanotti. Experimental study of the aerodynamic interaction between side-by-side propellers in evtol airplane mode through stereoscopic particle image velocimetry. *Aerospace*, 8(9), 2021.

[19] A. Colli, A. Zanotti, and G. Gibertini. Wind tunnel experiments on parallel blade–vortex interaction with static and oscillating airfoil. *Fluids*, 9(5), 2024.

[20] L. Riccobene, D. Grassi, J.N. Braukmann, M. Kerho, G. Droandi, and A. Zanotti. Wind tunnel test of full-scale wing-propeller system of a evtol aircraft. *The Aeronautical Journal*, 128(1324):1204–1218, 2024.

[21] C. Moreira and C. Breitsamter. Wind tunnel experiments of an evtol wing-propeller configuration. In *Proceedings of the Aerospace Europe Conference - EUCASS - CEAS - 2023*, 2023.

[22] C. Moreira, N. Herzog, and C. Breitsamter. Wind tunnel investigation of transient propeller loads for non-axial inflow conditions. *Aerospace*, 11(4), 2024.